By accounting for a certain degree of robustness to handle possible model uncertainties and external disturbances, the reduced dimension polytope, $\hat{\Theta}_R$, is defined by the ranges: $\hat{\rho}_1 \in [0.4, 2] \times 10^4$, $\hat{\rho}_2 \in [0.05, 0.35]$, and $\hat{\rho}_3 \in [-1, 2]$, as in Figure 3.6.

### 3.3.3   Controller Synthesis Results

The polytopic controller synthesis is formulated as the solution of the optimization problem in Propositions 3.3-3.4, by imposing the closed-loop performances defined in Section 3.3.1 at each vertex of the polytope. The polytope is defined through the reduced scheduling functions' ranges of variation, identified in Section 3.3.2. The control design results, discussed in this section, correspond to the final step of the iterative design process that allowed optimizing the dimensions of the polytope.

**Remark 3.8** (Numerical Conditioning)
*As discussed in [PV+11], the Feasibility LMIs conditions in Equation (3.11) are solved to find an optimal performance level, $\gamma^*$. In order to improve the numerical conditioning of the optimization, the conditions in Equation (3.11) are recomputed a second time, by imposing:*

$$\gamma = \gamma^* \left(1 + \zeta/100\right); \qquad and \qquad \begin{bmatrix} X & \varepsilon I_{n_{x_P}} \\ \varepsilon I_{n_{x_P}} & Y \end{bmatrix} \succ 0$$

*where $\zeta > 0$ is a tolerance percentage.*
*Thus, the recomputed optimization relies on the maximization of $\varepsilon > 0$. In this way, the minimal eigenvalues of $XY$ are maximized, avoiding bad conditioning related to the inversion of $M$ and $N$ during the controller Reconstruction in Proposition 3.4.*

The LPV/$\mathcal{H}_\infty$ polytopic design, performed by selecting $\zeta = 5$ and imposing a 5% tolerance level, provides an $\mathcal{H}_\infty$ performance level, $\gamma_\infty = 5.8$. The results are investigated in the frequency domain and are shown in Figures 3.7-3.8. Each figure represents a specific closed-loop
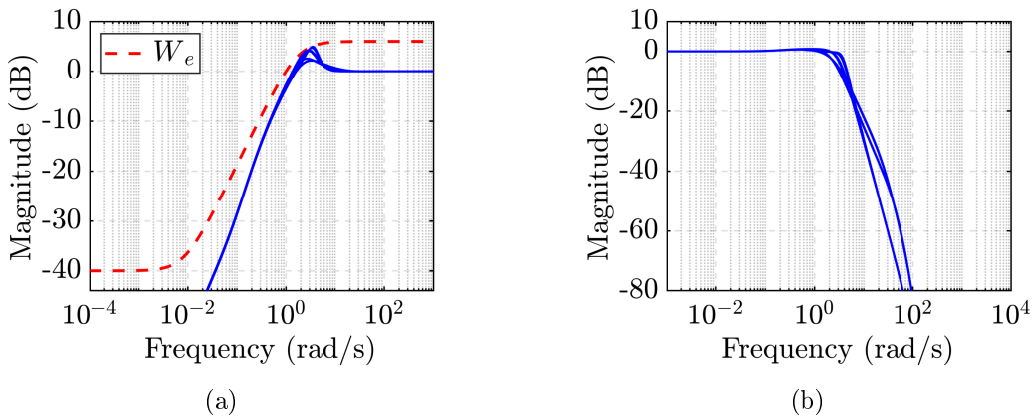


Figure 3.7: Polytopic design results: (a) Sensitivity functions; (b) Complementary Sensitivity functions.
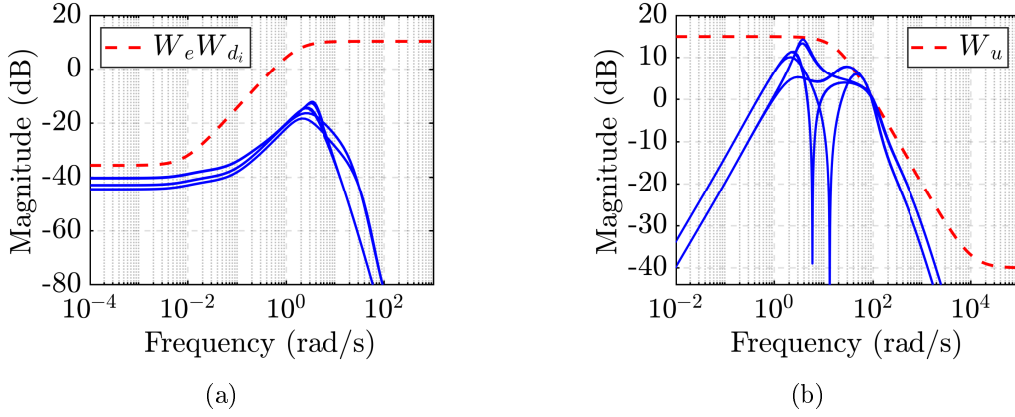
Figure 3.8: Polytopic design results: (a) Plant Sensitivity functions; (b) Controller Sensitivity functions.

property of the system, evaluated at each of the eight vertex conditions of the polytope (blue lines). As a first observation, Figure 3.7(a) shows how the peaks of the output Sensitivity functions, $S_y = \frac{e}{r}$, remain $\leq 6$ dB for each curve, ensuring reliable robustness margins at the vertices of the polytope. The transient dynamics of the system tends to be slightly less responsive due to the LMIs optimization that satisfies simultaneously the frequency requirements at each flight condition. However, the employment of the pair of weighting functions, $(W_e, W_r)$, successfully imposes a reasonable bandwidth to the output Sensitivity functions and considerably improves the low-frequency disturbance rejection capability of the system, as shown through the Plant Sensitive functions, $S_y G = \frac{e}{d_i}$, in Figure 3.8(a). The latter property is fundamental to guaranteeing the controller can handle not only the uncertainties introduced during the modeling and approximation procedures, but especially external disturbances affecting the operating conditions of the projectile (e.g. wind contributions).

Similarly, the polytopic design provides reliable high-frequency noise attenuation to handle possible distortions affecting the measurements, as shown in Figure 3.7(b). Indeed, the peaks of the Complementary Sensitivity functions are maintained at $\leq 1$ dB. Concerning the performances imposed on the control effort by the weighting function, $W_u$, the Controller Sensitivity functions, $KS_y = \frac{\dot{\delta}_{q,\mathrm{cmd}}}{r}$, respect the limitations at all the flight conditions, both in terms of the operating bandwidth and in terms of the low-frequency steady-state amplitude, as shown in Figure 3.8(b). The presence of the reference model increases the effort required by the actuators to provide the desired performance, but the limitations guarantee considerable margins from saturation occurrences.

As discussed in Section 3.2.3.3, the solution of the design corresponds to a set of LTI controllers, $K_{\hat{\theta}_i}$, with $i = 1, \cdots, 8$. In terms of implementation, for any combinations of the scheduling functions' values belonging to the polytope, the LPV polytopic controller, $K_{\mathrm{PY}}(\hat{\boldsymbol{\rho}})$, is obtained through the convex interpolation, $\mu_{\hat{\theta}_i}$, of the set of LTI vertices controllers as:

$$K_{\mathrm{PY}}(\hat{\boldsymbol{\rho}}) = \sum_{i=1}^{8} \mu_{\hat{\theta}_i}(\hat{\boldsymbol{\rho}}) K_{\hat{\theta}_i} \qquad \text{with:} \quad \sum_{i=1}^{8} \mu_{\hat{\theta}_i}(\hat{\boldsymbol{\rho}}) = 1.$$

## 3.4 Grid-Based Controller Design

This section is dedicated to the synthesis of the grid-based LPV controller, $K_{\mathrm{GR}}$, based on the projectile pitch channel quasi-LPV model derived in Section 2.3.2 of Chapter 2. The design objectives are presented first to derive the generalized scheme employed in the controller synthesis. The synthesis directly addresses the flight envelope defined by the scheduling variables' ranges of variation: $\alpha \in [0, 16]$ deg, $V \in [160, 280]$ m/s, and $h \in [1, 15]$ km.

The grid-based design relies on the resolution of the LMIs optimization, formulated in Theorem 3.3, at each flight point belonging to the selected design grid. The computational complexity affecting the optimization performance tends to exponentially increase with the number of the grid points, $n_{\mathrm{g}}$, and the number of scheduling variables, $n_{\rho}$, as $\mathcal{O}(n_{\mathrm{g}}^{n_{\rho}})$, as discussed in Section 3.2.2.1. Furthermore, no clear guidelines are provided in the selection of the grid points and the density level of the grid to ensure stability in the transient between two flight conditions, as explained in Remark 3.3. As a consequence, the projectile flight envelope is extensively investigated, aiming to identify the most critical flight conditions affecting the stability of the projectile dynamics. The core idea is to reduce the complexity of the optimization problem by restricting the grid points selection to the critical areas of the flight envelope. Additionally, the selection of the basis functions employed in the definition of the LMIs problem is analyzed, trying to accurately characterize the dependence of the projectile stability on each scheduling variable. Indeed, no general criteria are provided either for this latter aspect, as mentioned in Remark 3.2.

Finally, the results of the controller synthesis provide an overview of the corresponding closed-loop frequency properties.

### 3.4.1 Grid-Based Design Scheme

The overall design scheme is shown in Figure 3.9. Complying with the formulation in Equation (3.7), the generalized plant, $\Sigma_{\mathrm{P}}$, includes the projectile pitch channel quasi-LPV model, $\Sigma_{\mathrm{GR}}$, summarized in Equations (2.40)-(2.41) of Chapter 2, and accounting for load factor measurements. Additionally, $\Sigma_{\mathrm{P}}$ includes the second-order actuator model in Equation (1.39), and a set of weighing functions that shapes the $\mathcal{H}_{\infty}$ frequency properties of the desired closed-loop system. The first-order weighting functions, $W_e$ and $W_u$, target respectively the system tracking capability and the control effort performances. As for the polytopic case, the core objective consists of the minimization of the tracking error, $e = r - \alpha$, where the reference signal, $r$, is defined as an optimal AoA trajectory for LDR optimization purposes. The weighting functions are parameterized as follows:

$$W_e(s) = \frac{s/M_e + \omega_e}{s + \omega_e \epsilon_e}; \qquad W_u(s) = \frac{s + \omega_u/M_u}{\epsilon_u s + \omega_u}$$

where the high-frequency gain, $M_e = 2$, the low-frequency gain, $\epsilon_e = 0.01$, and the crossover frequency, $\omega_e = 1$ rad/s, guarantee 6 dB of module margin, improving the robustness of the
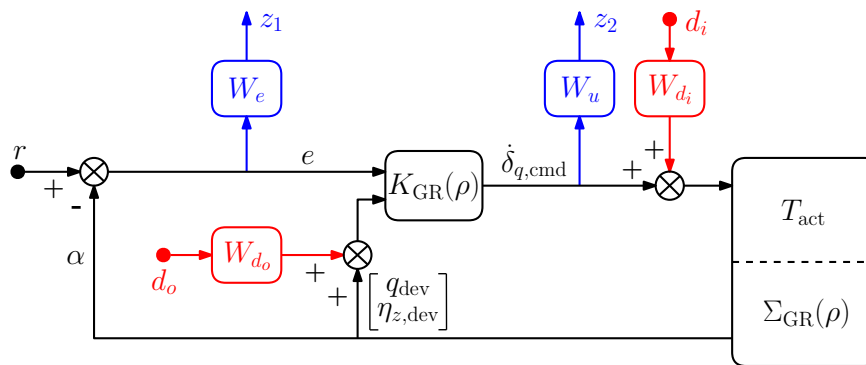
Figure 3.9: Grid-based design scheme architecture.

system, -40 dB of disturbance signals attenuation, and a steady-state tracking error $\leq 1\%$ at low frequency, respectively. Concerning the control signal, $\epsilon_u = 0.01$ and $\omega_u = 100$ rad/s provide an additional -40 dB of high-frequency noise attenuation, and an input bandwidth that complies with the actuator operating limitations. Finally, a low-frequency gain, $M_u = 3$, is imposed on the control signal amplitude.

Differently from the polytopic approach, the grid-based design relies on a parameter-dependent solution of the control problem in Proposition 3.2. At the expense of robust stability guarantees only around the design points instead of broader quadratic stability properties, the optimization can more optimally target each specific flight condition, providing higher computation performance. In this context, the tracking capability and the disturbance rejection of the system can be mutually handled by the single weighting function, $W_e$, avoiding the employment of an additional reference model/filter. However, the enhancement of the tracking capability may increase the sensitivity of the system to disturbance signals, thus a reliable trade-off has to be achieved avoiding the imposition of an excessive control effort and the consequent occurrence of possible canards stall regime.

Finally, constant weights, $W_{d_i} = 0.6$ and $W_{d_o} = 0.2$, are imposed on the input and output disturbance signals, $d_i$ and $d_o$, respectively, to improve the controller disturbance rejection, and to satisfy the controller synthesis orthogonality conditions ([Wu95]). The observations discussed in Remark 3.7, concerning the limited performance related to the employment of parameter-independent weighting functions, apply also to the grid-based design.
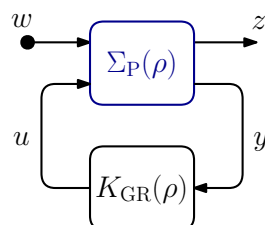


Figure 3.10: General grid-based control scheme configuration.

The generalized control architecture is presented in Figure 3.10, where the generalized state vector, $\boldsymbol{x}_{\mathrm{P}} = [\boldsymbol{x}^{\mathrm{T}}, \boldsymbol{x}_{\mathrm{act}}^{\mathrm{T}}, x_{W_e}, x_{W_u}]^{\mathrm{T}} \in \mathbb{R}^9$, of the open-loop plant, $\Sigma_{\mathrm{P}}(\boldsymbol{\rho})$, defined in Equation (3.7), accounts for the projectile quasi-LPV model, $\boldsymbol{x} = [\alpha, q_{\mathrm{dev}}, \delta_{q,\mathrm{dev}}]^{\mathrm{T}} \in \mathbb{R}^3$, the actuator dynamics, and the weighting functions. The generalized controlled output, $\boldsymbol{z} = [z_1, z_2]^{\mathrm{T}} \in \mathbb{R}^2$, includes the design objectives, while tracking error, off-equilibrium pitch rate, and off-equilibrium load factor, define the available measurements set, $\boldsymbol{y} = [e, q_{\mathrm{dev}}, \eta_{z,\mathrm{dev}}]^{\mathrm{T}} \in \mathbb{R}^3$. Finally, the control input, $u \in \mathbb{R}$, is the derivative of the commanded local pitch deflection, $\dot{\delta}_{q,\mathrm{cmd}}$, while the vector of exogenous input, $\boldsymbol{w} = [r, d_i, d_o]^{\mathrm{T}} \in \mathbb{R}^3$, includes the reference guidance AoA trajectory, and the input/output disturbance signals.

The generalized plant is evaluated at each grid point condition. The obtained set of $n_{\mathrm{g}}$ LTI systems is employed for the controller synthesis in the resolution of the LMIs problem formulated in Theorem 3.3.

## 3.4.2 Grid Design Analysis

The investigated grid-based control design relies on the conversion of an infinite-dimensional LMIs problem into a solvable SDP optimization. As discussed in Section 3.2.2.1, the conversion is based on two relaxation steps:

**I. Projection** of the infinite-dimensional decision variables into a finite set of basis functions, as in Theorem 3.1.

**II. Discretization (gridding)** of the scheduling variables space into a finite set of conditions, as in Proposition 3.1.

As a consequence, the proper formulation of the controller synthesis in Theorem 3.3 is based on the accurate selections of both the set of basis functions and the set of discretized conditions. However, as stated in Remarks 3.2-3.3, no precise general guidelines are provided for any of the selections, requiring the employment of more case-dependent approaches. Additionally, the computational complexity affecting the performance of the optimization tends to increase with the number of grid points, as $\mathcal{O}(n_{\mathrm{g}}^{n_\rho})$. Since the design guarantees robust stability only around the selected grid points, a compromise has to be reached between a reliable dimension of the grid, and the resulting complexity of the overall computation.

In order to improve the performance of the controller synthesis, an exhaustive analysis is developed, investigating the following aspects:

**A. Flight Envelope:** analyze the scheduling variables space to identify the most critical flight conditions affecting the stability properties of the projectile quasi-LPV pitch channel dynamics. The objective is to restrict the area of selection of the design grid points to those characterized by critical stability conditions. Additional considerations about the projectile optimal desired trajectory allow for a more accurate selection.

**B. Optimization Performance:** estimate the effect of the number of grid points, $n_g$, and basis functions selections on the computational complexity and on the performance of the controller synthesis optimization.

### 3.4.2.1 A. Flight Envelope Analysis

The identification of the critical areas of the flight envelope relies on the analysis of the pole-zero map of the projectile quasi-LPV model in Equations (2.40)-(2.41). The analysis targets the full ranges of variation of the scheduling variables: $\alpha \in [0, 16]$ deg, $V \in [160,$
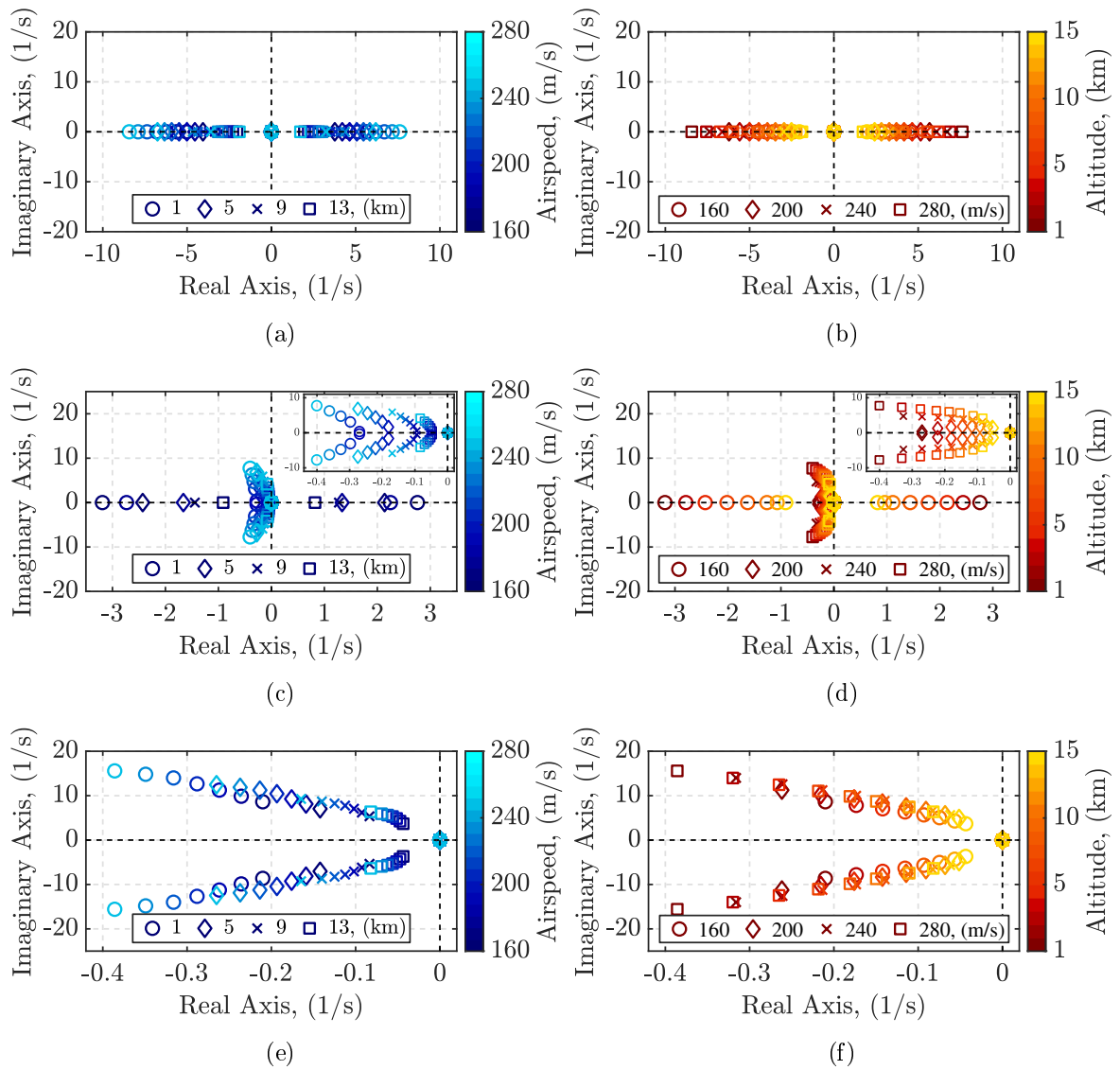


Figure 3.11: Dynamics dependence on the airspeed and altitude variations at: (a)-(b) $\alpha = 5$ deg, respectively; (c)-(d) $\alpha = 9$, respectively; (e)-(f) $\alpha = 13$ deg, respectively.

280] m/s, and $h \in [1, 15]$ km, assuming the corresponding discretization steps: $\Delta\alpha = 1$ deg, $\Delta V = 5$ m/s, and $\Delta h = 500$ m, for a total of $n_g = 12750$ grid points. The results in Figure 3.11 provide samples of the complete analysis at selected flight conditions. In particular, Figures 3.11(a)(c)(e) show how the system dynamics varies at certain altitude levels and as a continuous function of the airspeed, respectively, at $\alpha = 5$ deg, at $\alpha = 9$ deg, and $\alpha = 13$ deg. The same results are provided also in Figures 3.11(b)(d)(f), where the attention is focused on the stability dependence on the continuous altitude variation.

The results are employed to derive a 3D stability envelope in the discretized space of the scheduling variables, as shown in Figure 3.12. The stability map targets only a subset of the AoA range, $\alpha \in [5, 10]$ deg, characterized by the transition from unstable to stable dynamics. Indeed, for $\alpha \geq 10$ deg, the system is stable at any $(V, h)$ conditions, while for $\alpha \leq 5$ deg, the system is always unstable. As a general result, the system dynamics tends toward a progressively more unstable behavior for decreasing values of the airspeed and altitude levels. As expected, the AoA variation has the most relevant effect on the system stability.

**Remark 3.9**
*The pole-zero stability evaluation relies on the quasi-LPV model of the projectile pitch channel dynamics. Thus, the accuracy of the results in representing the dynamics of the original nonlinear system is limited to the domain of reliability of the quasi-LPV model. However, the dynamics stability transition shown in Figure 3.12 is coherent with the stability considerations discussed in Section 1.3.2.2 of Chapter 1 through the analysis of the aerodynamic pitching moment CFD data.*
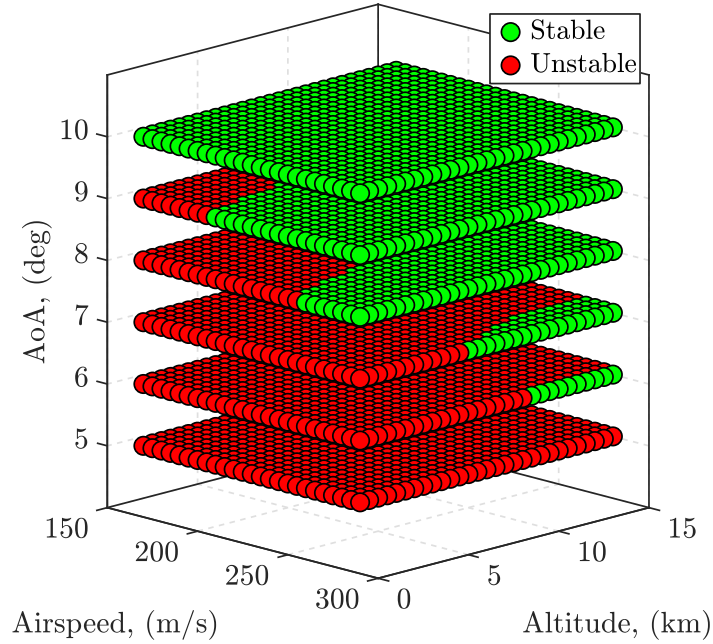


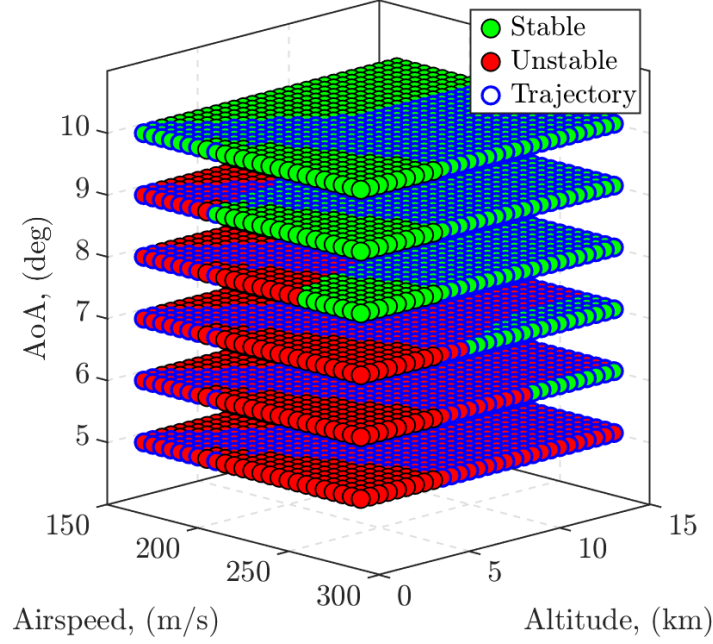Figure 3.12: 3D discretized system's stability envelope.

Figure 3.13: Reduced stability envelope based on trajectory considerations.

In order to further restrict the area of selection of the design points, trajectory performance restrictions can be employed. In the polytope mapping procedure developed in Section 2.4.2 of Chapter 2, the **Selection** step consisted of the definition of specific trajectory criteria for the identification of the new convex space. The objective was to restrict the investigated flight envelope to those areas that respect the physical constraints characterizing the scheduling variables across a desired projectile gliding trajectory. By applying the same criteria to the obtained stability results, the critical flight envelope can be reduced, as in Figure 3.13.

### 3.4.2.2   B. Optimization Performance Analysis

The second part of the analysis aims to estimate the impact of the number of selected grid points, $n_{\mathrm{g}}$, on the optimization performance and on the computational time, $t_{\mathrm{eval}}$. Additionally, the analysis investigates the relevance of the basis functions, $f_i(\boldsymbol{\rho})$ and $g_i(\boldsymbol{\rho})$ with $i = [1, \ldots, n_{\mathrm{B}}]$, selected for each scheduling variable to define the Lyapunov functions, $X(\boldsymbol{\rho})$ and $Y(\boldsymbol{\rho})$, parameterized as in Equation (3.8).

**Assumption 3.3**
*In order to simplify the computation, the same set of basis functions is employed to characterize both $X(\boldsymbol{\rho})$ and $Y(\boldsymbol{\rho})$ parameterizations, thus: $f_i(\boldsymbol{\rho}) = g_i(\boldsymbol{\rho})$ with $i = [1, \ldots, n_{\mathrm{B}}]$.*

The analysis consists of the resolution of the LPV $\mathcal{H}_\infty$ controller synthesis problem in Proposition 3.2, assuming the generalized design scheme defined in Section 3.4.1. The opti-

mization problem is formulated by accounting for one single parameter variation at a time, imposing frozen values for the remaining ones. Thus, three individual analyses are performed, as summarized in Table 3.1.

Table 3.1: Optimization analyses conditions.

| **Analyzed Variable** | $\alpha$ **(deg)** | $V$ **(m/s)** | $h$ **(km)** |
|:---:|:---:|:---:|:---:|
| $\boldsymbol{\alpha}$ | $\in [0, 16]$ | 230 | 7 |
| $\boldsymbol{V}$ | 9 | $\in [160, 280]$ | 7 |
| $\boldsymbol{h}$ | 9 | 230 | $\in [1, 15]$ |

For each analyzed variable, the $\mathcal{H}_\infty$ optimization is evaluated by progressively increasing the number of grid points that discretize the corresponding variation range in Table 3.1. At each increment of $n_\mathrm{g}$, the discretized set of grid points is augmented by randomly selecting a new point in the range of variation. The resulting performance level, $\gamma_\infty$, is employed as a comparison index to estimate the impact of the $n_\mathrm{g}$ increment on the quality of the optimization solution. The computation is repeated several times, $n_\mathrm{exp}$, for statistical relevance, accounting for different permutations of the same set of grid points. The average value of each full repetitions set is shown as a global result.

In order to account for the relevance of the basis functions, the full procedure is repeated by employing different sets, $\boldsymbol{f}_\mathrm{B}$, for each scheduling variable, selected based on the mimic principle. The evaluation of the computational time at each iteration of the process provides an index of the optimization complexity increment generated by the grid points and basis functions' selections. The overall procedure is detailed in Algorithm 3.

---

**Algorithm 3** Optimization Performance Analysis

---

**For** any $\rho \in [\alpha, V, h]$:

> Select the initial analysis range: $\mathrm{R}_\rho = [\rho_\mathrm{min}, \rho_\mathrm{max}]$.

> Select constant values for the remaining variables.

> **For** $j = [1, \ldots, n_\mathrm{exp}]$:

>> **For** $n_\mathrm{g} = [3, \ldots, 13]$:

>>> Select a new random grid point: $\mathtt{rand}(\rho_i) \in [\rho_\mathrm{min}, \rho_\mathrm{max}]$.

>>> Redefine $\mathrm{R}_\rho = [\mathrm{R}_\rho, \mathtt{rand}(\rho_i)]$.

>>> **For** any set $\boldsymbol{f}_\mathrm{B}$:

>>>> $[t_\mathrm{eval}, \gamma_\infty] = f[\text{Controller Synthesis}](\mathrm{R}_\rho, \boldsymbol{f}_\mathrm{B})$, as in Theorem 3.3.

>>> **end**.

>> **end**.

>> Reset the initial range: $\mathrm{R}_\rho = [\rho_\mathrm{min}, \rho_\mathrm{max}]$.

> **end**.

**end**.

---

The sets of basis functions investigated for each scheduling variable are listed respectively in Tables 3.2-3.3-3.4.

Table 3.2: Basis functions sets: AoA.

| Basis Set ($\boldsymbol{\alpha}$) | $\boldsymbol{f_1}$ | $\boldsymbol{f_2}$ | $\boldsymbol{f_3}$ |
|:---:|:---:|:---:|:---:|
| $\boldsymbol{f}_{\mathrm{B_1}}$ | 1 | $\alpha$ | $-$ |
| $\boldsymbol{f}_{\mathrm{B_2}}$ | 1 | $\alpha$ | $\sin\alpha$ |
| $\boldsymbol{f}_{\mathrm{B_3}}$ | 1 | $\alpha$ | $\cos\alpha$ |
| $\boldsymbol{f}_{\mathrm{B_4}}$ | 1 | $\sin\alpha$ | $\cos\alpha$ |

Table 3.3: Basis functions sets: airspeed.

| Basis Set ($\boldsymbol{V}$) | $\boldsymbol{f_1}$ | $\boldsymbol{f_2}$ | $\boldsymbol{f_3}$ |
|:---:|:---:|:---:|:---:|
| $\boldsymbol{f}_{\mathrm{B_1}}$ | 1 | $V$ | $-$ |
| $\boldsymbol{f}_{\mathrm{B_2}}$ | 1 | $V$ | $1/V$ |
| $\boldsymbol{f}_{\mathrm{B_3}}$ | 1 | $V$ | $V^2$ |

Table 3.4: Basis functions sets: altitude.

| Basis Set ($\boldsymbol{h}$) | $\boldsymbol{f_1}$ | $\boldsymbol{f_2}$ | $\boldsymbol{f_3}$ |
|:---:|:---:|:---:|:---:|
| $\boldsymbol{f}_{\mathrm{B_1}}$ | 1 | $h$ | $-$ |
| $\boldsymbol{f}_{\mathrm{B_2}}$ | 1 | $h$ | $1/h$ |
| $\boldsymbol{f}_{\mathrm{B_3}}$ | 1 | $h$ | $h^2$ |

The results of the analyses are presented in Figure 3.14. In particular, Figures 3.14(a)(c)(e) show the average $\gamma_\infty$ performance level obtained across $n_{\mathrm{exp}} = 100$ different optimizations on each basis functions set, $\boldsymbol{f}_{\mathrm{B}_i}$, respectively performed on the $\alpha$, $V$, and $h$ variation ranges. The corresponding average computational time curves are shown in Figures 3.14(b)(d)(f). As a first general observation, $t_{\mathrm{eval}}$ tends to linearly grow with increasing values of $n_{\mathrm{g}}$ in all the optimization scenarios. However, the number, $n_{\mathrm{B}}$, and the complexity of the basis functions set also play a relevant role in terms of performance, since they can easily double the time required to achieve an optimal solution.

**AoA Analysis.** Concerning the performance level, the employment of the basis functions sets, $\boldsymbol{f}_{\mathrm{B_3}}$ and $\boldsymbol{f}_{\mathrm{B_4}}$ in Table 3.2, provides nearly the same results, as shown in Figure 3.14(a). The $\gamma_\infty$ values increase when the least complex basis set, $\boldsymbol{f}_{\mathrm{B_1}}$, is considered, while the best optimization results rely on $\boldsymbol{f}_{\mathrm{B_2}}$. Coherently with the expectations, $\boldsymbol{f}_{\mathrm{B_3}}$ and $\boldsymbol{f}_{\mathrm{B_4}}$ show a linear increase of the $\gamma_\infty$ index w.r.t. $n_{\mathrm{g}}$, since it directly affects the number of LMIs to be solved by the optimization. However, due to the highly nonlinear parameterization, the same dependence is not clearly highlighted by the curves related to $\boldsymbol{f}_{\mathrm{B_1}}$ and $\boldsymbol{f}_{\mathrm{B_2}}$. Thus, a global intuition on the relevance of $n_{\mathrm{g}}$ to the optimization problem is not reachable. In terms of computational complexity, the $t_{\mathrm{eval}}$ related to $\boldsymbol{f}_{\mathrm{B_2}}$ in Figure 3.14(b) is coherently more than twice larger than the simplest set $\boldsymbol{f}_{\mathrm{B_1}}$, while $\boldsymbol{f}_{\mathrm{B_3}}$ and $\boldsymbol{f}_{\mathrm{B_4}}$ seem to offer a preferable trade-off between performance and computational time.

**Airspeed Analysis.** The curves in Figure 3.14(c) and Figure 3.14(d) highlight a similar behavior for $\gamma_\infty$ and $t_{\mathrm{eval}}$ compared to the AoA case. Indeed, the simplest set, $\boldsymbol{f}_{\mathrm{B_1}}$ in Table 3.3, is characterized by a linear $\gamma_\infty/n_{\mathrm{g}}$ relation, and a lower computational complexity, respectively. The higher nonlinear parameterization selected for the basis functions sets, $\boldsymbol{f}_{\mathrm{B_2}}$ and $\boldsymbol{f}_{\mathrm{B_3}}$, results

in increasingly higher but less predictable performance levels. Accordingly, the computational time necessary to perform the optimization is twice as large as the linear case. As a general observation, $\gamma_\infty$ achieves the desired objective, $0 < \gamma_\infty < 1$, at almost all the conditions.
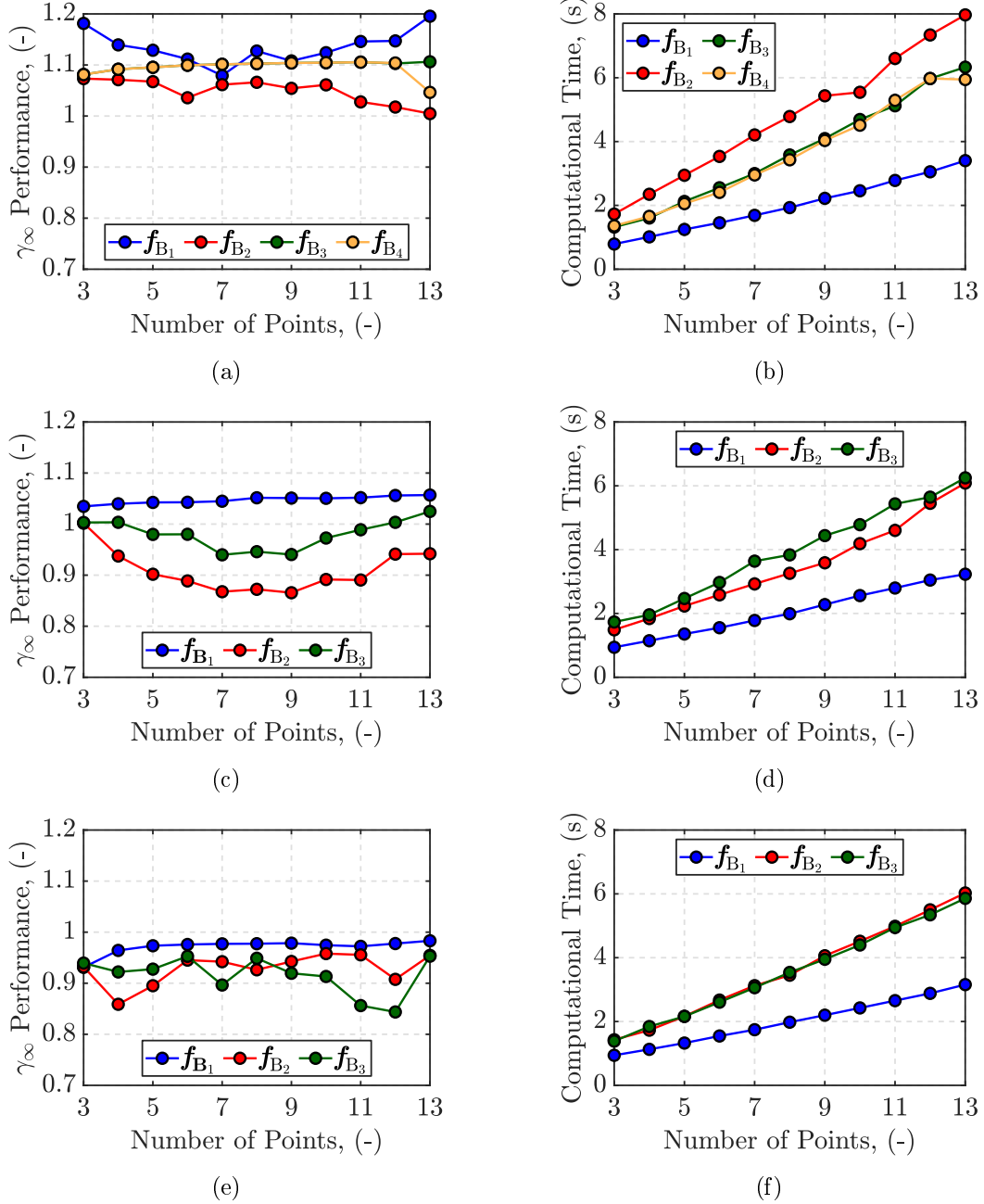


Figure 3.14: Performance level and computational time dependence on the grid points and basis functions selections: (a)-(b) AoA analysis, respectively; (c)-(d) airspeed analysis, respectively; (e)-(f) altitude analysis, respectively.

**Altitude Analysis.** The altitude analysis results in Figure 3.14(e) provide the highest optimization performance, ensuring $\gamma_\infty < 0$ for all the sets of basis functions. As for the airspeed case, $\boldsymbol{f}_{B_1}$ is the only set characterized by a linear performance dependence on the $n_g$ increment. Coherently, the computational complexity is minimized only in the linear case.

### 3.4.3 Controller Synthesis

The grid analysis provides a clearer understanding of the system properties and the relevance of each scheduling variable on the overall controller optimization. The results allow for reducing the computational complexity of the process and improving the performance by focusing the design on a critical subset of the flight envelope.

Considering both the $\gamma_\infty$ and $t_{eval}$ performances in Figure 3.14, the ranges of each scheduling variable are discretized into following finite sets of flight conditions: $\boldsymbol{\alpha}_{grid} = [1, 5, 8, 13]$ deg, $\boldsymbol{V}_{grid} = [180, 200, 240, 270]$ m/s, and $\boldsymbol{h}_{grid} = [3, 6, 9, 12, 14.5]$ km. Additionally, the grid-based design accounts for the variation rates of the scheduling variables, as mentioned in Remark 3.1. The stricter the conditions imposed to variation rates, the higher the performance of the optimization[1]. The estimation of the scheduling variables max/min variation rates relies on reference gliding phase trajectory simulations: $\dot{\alpha}_{grid} \in [-30, 30]$ deg/s, $\dot{V}_{grid} \in [-50, 50]$ m/s$^2$, and $\dot{h}_{grid} \in [-100, 100]$ m/s.

The controller synthesis is performed using the LPVTools MATLAB Toolbox ([HSP15]), employing the LMI-Lab optimization solver ([Gah+94]).

**Remark 3.10**
*A relevant functionality limitation of LPVTools concerns the possibility of defining only rectangular grids of discretized scheduling variables. Thus, given two scheduling variables' discretized sets, $\boldsymbol{a} = [a_1, \ldots, a_N]$ and $\boldsymbol{b} = [b_1, \ldots, b_M]$, the corresponding grid is generated as the Cartesian product, $\boldsymbol{a} \times \boldsymbol{b} = \{(a_i, b_j) \mid a_i \in \boldsymbol{a} \text{ and } b_j \in \boldsymbol{b}\}$. As a consequence, the selection and the number of flight conditions are partially limited by the definition of the grid, introducing a certain level of conservatism and unwanted complexity in the controller synthesis.*

Based on the results of the grid analyses and accounting for the limitation discussed in Remark 3.10, the Cartesian product between the discretized scheduling variables sets generates a design grid, $\Xi = \boldsymbol{\alpha}_{grid} \times \boldsymbol{V}_{grid} \times \boldsymbol{h}_{grid}$, of $n_g = 80$ flight points, unevenly distributed across the 3D flight domain. The employment of unevenly distributed grid points, targeting the most critical areas of the operating domain, is expected to improve the stability guarantees of the controller synthesis. Concerning the selection of the basis functions, the compromise between performance and complexity leads to the following definition of the parameterized Lyapunov functions in Equation (3.8), accounting for the simplification in Assumption 3.3:

$$X(\boldsymbol{\rho}) = Y(\boldsymbol{\rho}) = X_0 + X_{\alpha,1} \sin \alpha + X_{\alpha,2} \cos \alpha + X_V V + X_h h.$$

---

[1]The polytopic design allows for an infinite variation of each scheduling variables since no limitations are imposed in the LMIs formulation, providing more conservative results but higher stability guarantees.